SANDIA REPORT
SAND2001-0897
Unlimited Release
Printed April 2001

Photonics Integration Devices and Technologies

G. Allen Vawter, Shawn Lin, Charles Sullivan, Walt Zubrzycki, Weng Chow, Andy Allerman, and Joel Wendt

Prepared by
Sandia National Laboratories
Albuquerque, New Mexico 87185 and Livermore, California 94550

Sandia is a multiprogram laboratory operated by Sandia Corporation, a Lockheed Martin Company, for the United States Department of Energy under Contract DE-AC04-94AL85000.

Issued by Sandia National Laboratories, operated for the United States Department of Energy by Sandia Corporation.

Available to DOE and DOE contractors from
U.S. Department of Energy
Office of Scientific and Technical Information
P.O. Box 62
Oak Ridge, TN 37831

Telephone: (865)576-8401
Facsimile: (865)576-5728
E-Mail: reports@adonis.osti.gov
Online ordering: http://www.doe.gov/bridge

Available to the public from
U.S. Department of Commerce
National Technical Information Service
5285 Port Royal Rd
Springfield, VA 22161

Telephone: (800)553-6847
Facsimile: (703)605-6900
E-Mail: orders@ntis.fedworld.gov
Online order: http://www.ntis.gov/ordering.htm

SAND2001-0897
Unlimited Release
Printed April 2001

Photonics Integration Devices and Technologies

G. Allen Vawter
Advanced Materials and Devices Research and Development

Shawn Lin, Charles Sullivan
Photonics and Microfabrication

Walt Zubrzycki
Advanced Materials and Devices Research and Development

Weng Chow
Semiconductor Materials and Device Sciences Department

Andy Allerman
Advanced Materials and Devices Research and Development

Joel Wendt
Photonics and Microfabrication

Sandia National Laboratories
P. O. Box 5800
Albuquerque, NM 87185-0603

Abstract

We have used selective AlGaAs oxidation, dry-etching, and high-gain semiconductor laser simulation to create new in-plane lasers with interconnecting passive waveguides for use in high-density photonic circuits and future integration of photonics with electronics. Selective oxidation and doping of semiconductor heterostructures have made vertical cavity surface emitting lasers (VCSELs) into the world's most efficient low-power lasers. We apply oxidation technology to improve edge-emitting lasers and photonic-crystal waveguides, making them suitable for monolithic integrated microsystems. Two types of lasers are investigated: 1) a ridge laser with resonant coupling to an output waveguide; 2) a selectively-oxidized laser with a low active volume and potentially sub-milliAmp threshold current. Emphasis is on development of high-performance lasers suited for monolithic integration with photonic circuit elements.

Acknowledgment

The authors thank Edmond Chow, Chuck Alford, Tom Plut, Denise Tibbetts, Chuck Fuller, Tom Bauer and Ron Hadley at Sandia National Labs for technical assistance.

This work was supported by United States Department of Energy under Contract DE-AC04-94AL85000. Sandia is a multiprogram laboratory operated by Sandia Corporation, a Lockheed-Martin Company, for the United States Department of Energy.

Contents

Figures

Nomenclature

VCSEL	Vertical Cavity Surface Emitting Laser
GRINSCH	Graded-index separate-confinement heterostructure
Q	resonant quality of a laser cavity
PIC	Photonic integrated circuit
OEIC	Optoelectronic integrated circuit
Γ	co-ordinate axis of crystal momentum
X	co-ordinate axis of crystal momentum
M	co-ordinate axis of crystal momentum
J_{th}	lasing threshold current density
I_{th}	lasing threshold current
QCSE	Quantum Confined Stark Effect
MQW	Multiple Quantum Well
SQW	Single Quantum Well
BOW	Buried optical waveguide
RIBE	Reactive ion beam etching
PMMA	a polymer for electron-beam lithography
p-type	semiconductor conducting via positive effective charge
n-type	semiconductor conducting via negative effective charge
dB	logarithmic unit of relative power
REM	resonantly enhanced mirror
R	reflectivity of mirror
L-I-V	light-current-voltage
L	laser length
λ	lamda, wavelength of light
d	hole diameter
a	photonic crystal lattice constant
t	film thickness
n	refractive index
ω	angular frequency
2D	two-dimensional
3D	three-dimensional
TM	transverse magnetic optical polarization
TE	transverse electric optical polarization
C	speed of light
NA	optical numerical aperture
IR	infrared
T	optical transmittance
N	integer number of lattice periods

ps	10^{-12} seconds
ns	10^{-9} seconds
μs	10^{-6} seconds
W	Watts, SI unit of power

meV	10^{-3} electron volts, unit of energy	μm	10^{-6} meters
cm^{-2}	inverse square centimeters	mm	10^{-3} meters
mA	10^{-3} Amperes current	A	Ampere, SI unit of current
GB	10^{9} bits of data	V	Volt, SI unit of electric potential
nm	10^{-9} meter	s	second, SI unit of time
m	meter, SI unit of length	cm^{2}	square centimeters
pA	10^{-12} Amperes	cm^{-1}	inverse centimeters

Background and Motivation

Several new applications are emerging in nuclear safety, NASA, and IWFO integrated microsystems projects that require monolithic integration of in-plane lasers coupled through low loss waveguides into other similar lasers or photodetectors. These applications require sub-mA laser threshold currents, high wall-plug efficiency, and small area for high-density integration and total-dose radiation hardness, i.e., VCSEL-like performance in a format integratable with other in-plane optical components. At present, the performance of etched-facet edge-emitting lasers in the (Al, Ga, In) As material system must be improved by more than an order of magnitude to adequately address our future system needs and develop new integrated microsystem business. For example, all-optical architectures for data processing are capable of ultra-fast (100 GB/s) computations performed on many parallel data streams provided that high-density monolithic integration of active and passive photonic devices is available. However, active (emitters) and passive (modulators and interconnects) photonic device design and process technologies are not capable of producing the high device density, high efficiency, and low power consumption needed to fabricate circuits with hundreds or thousands of devices per chip.

The key technical challenges which must be addressed in order to construct such high-efficiency, small volume in-plane laser/waveguide systems are the creation of small high-Q (Fabry-Perot resonator figure-of-merit, energy stored divided by the energy lost per cycle) optical cavities, generation of high modal gain, and efficient coupling between the laser and passive waveguide. High-Q cavities require the combination of low optical losses within the resonator and high reflectivity mirrors. High modal gain specifies a combination of nearly perfect injected current confinement within the gain medium and laser waveguide, large material gain in the active layer(s), and high confinement factor of the light within the gain medium. Efficient coupling from the laser to the waveguide requires low optical divergence of the laser output light. This low optical divergence must be balanced against the small mode size needed for low threshold.

Sandia has a uniquely powerful set of resources that may be applied to low-threshold in-plane laser technology. Drawing on our technology for photonics, VCSELs, and dry etching of nanostructures and facets, novel thin multi-layers of Al-oxide will be combined with artificially-engineered etched mirrors, including photonic bandgap structures, creating ultra-low-threshold, high efficiency edge-emitting lasers. These ultra-efficient lasers will require oxide engineering for combined optical mode and carrier control and loss minimization. Our nanostructure fabrication technology will be used to build in-plane waveguides based on photonic lattice artificial materials. The result of this three-year project will be new high efficiency lasers and laser-to-waveguide coupling systems suitable for high-density and low power monolithic integrated microsystems.

During the course of this LDRD program, we have applied Sandia's world-class expertise in selective AlGaAs oxidation, dry-etching, and high-gain GRINSCH MQW laser simulation to create new in-plane lasers and interconnecting passive waveguides for use in high-density photonic circuits and future integration of photonics with electronics. The project was terminated for non-technical reasons prior to integration of active lasers and detectors with passive waveguide interconnects.

Highly Efficient Buried Oxide Waveguide Lasers

Waveguide-based photonic integrated circuits (PICs) offer many attractive features, such as single-mode waveguides, couplers, and switches making them useful for optical computing and signal processing. However, the most highly capable circuits will take advantage of the best of electronics and photonics while avoiding the drawbacks of each technology. In this scenario, the electrical-to-optical interface will be high-speed, high-efficiency lasers diodes. Future realization of high-density or low-power opto-electronic integrated circuits (OEICs) will require extremely efficient light sources in order to reduce overall circuit power consumption. We report highly efficient, low-threshold-current edge-emitting lasers where both the optical waveguide and lateral current confinement are achieved by lateral selective oxidation of AlGaAs. This buried-oxide waveguide (BOW) laser structure employs lateral oxidation of AlGaAs layers above and below the active region resulting in an easily manufactured laser with a very small lateral optical mode size and high current confinement. Such highly confined lasers are well suited for OEIC applications where threshold current and overall efficiency are paramount. External differential quantum efficiency in excess of 95% and 40% wall-plug efficiency are demonstrated in devices without facet coatings.

Selective wet oxidation of Al[1] offers a powerful capability to simultaneously create both an optical waveguide and current aperture within a heterostructure of Al-containing compound semiconductors. Since the initial development of wet AlGaAs oxidation methods,[2] a number of oxidized edge-emitting laser concepts have been tried.[3] The most successful of these have used lateral selective oxidation of AlGaAs layers between 100 and 300 nm thickness. These layers have been used as current restricting apertures[4, 5] or for both current restriction and lateral waveguiding.[6-8] Use of an oxide layer above and below the laser active region offers the ability to create a self-aligned waveguide with current apertures on both sides of the pn-junction in a process requiring only one epitaxial growth step. The high refractive-index contrast between AlGaAs and its oxide permits fairly thin selectively-oxidized layers to form a very highly-confining optical waveguide. Such highly-confined waveguides with self-aligned current apertures are expected to give very low threshold currents and very high overall efficiency in an optimized laser design. Previous use of apertures for these dual purposes resulted in multi-moded lasers with reduced efficiency and elevated threshold current density due to non-ideal formation of the waveguide and possibly excess stress caused by the thick (300 nm) oxide layer.[6]

The BOW laser structure is shown in Fig. 1.1(a). Four oxide layers are shown extending laterally from the edges of a deeply-etched mesa. The optical mode of the laser cavity is pinched between the tips of the oxide layers and current injected from a large-area contact above the laser is funneled through the narrow oxide aperture. The BOW laser design has high optical and current confinement resulting from optimized placement of the oxide layers and selection of the aperture width. Fig. 1.1(b) is a numerical simulation of the optical mode overlaid onto the layer structure of the guide showing the strong lateral guiding effect of the

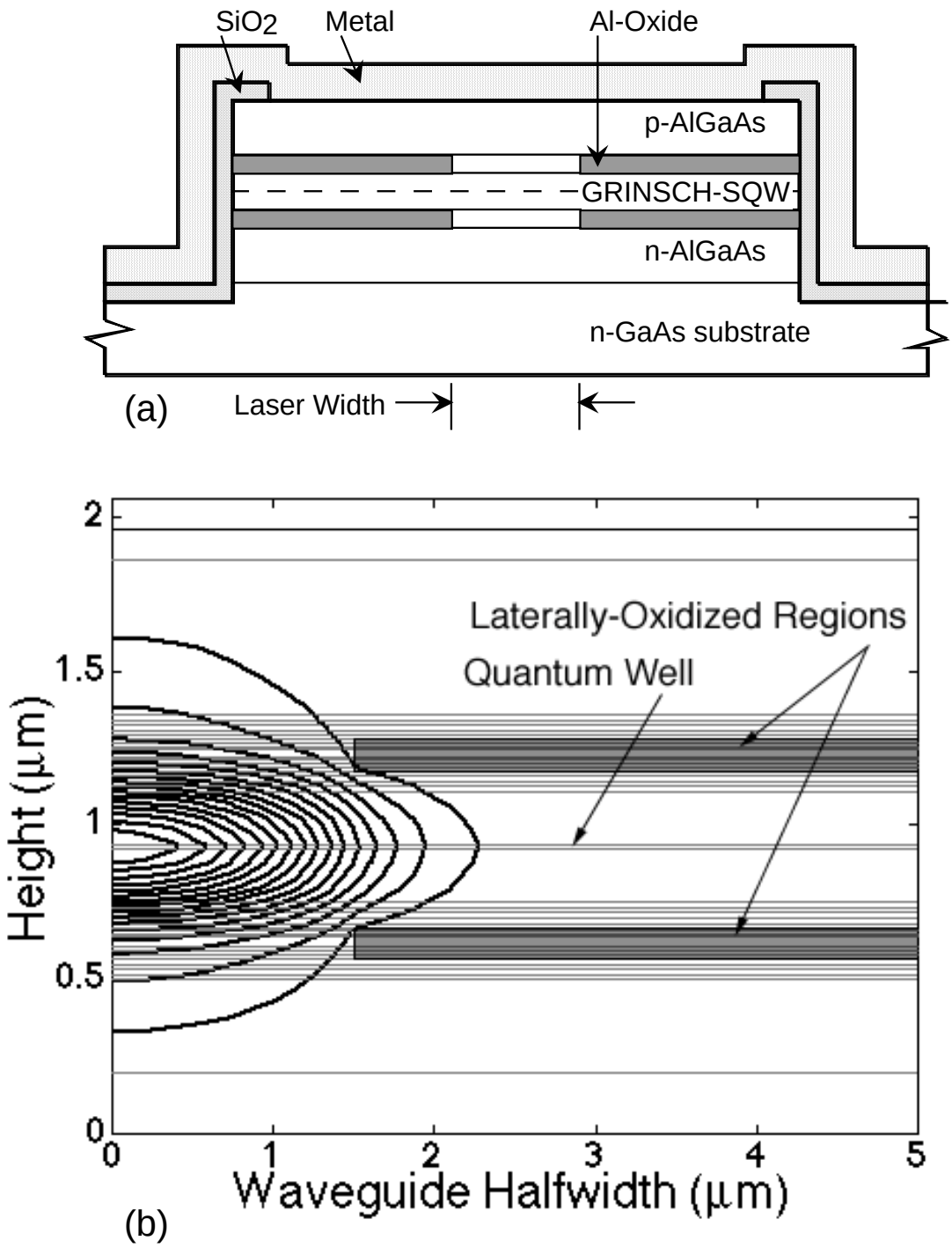

Figure 1.1: (a) Cross-section schematic of BOW laser showing location of laterally-oxidized regions above and below the GRINSCH-SQW layers. (b) Simulated contours of constant optical field overlayed onto the epitaxial structure of the BOW laser. Confinement of the optical (TE) mode by the GRINSCH structure in the vertical direction and the oxide layers in the horizontal direction is evident.

oxide layers. This design supports only one guided TE mode for laser widths less than 2 μm. Oxidation-induced stress is reduced by the use of thin, 40 nm, $Al_{0.98}Ga_{0.02}As$[1] oxidation layers. The minimum layer thickness was chosen in order to achieve a reproducible oxidation rate. Thinner oxidation layers may be used while maintaining the strong waveguiding effect although a reduced and oxidation rate may occur.

A key aspect of design of a BOW laser for high efficiency is the potential barrier created by the heterojunction offset between the oxidation layer, having as much as 98% Al content, and the surrounding waveguide cladding, where Al content does not usually exceed 60%. Reduction of these barriers through engineered grading and doping of the heterojunction has improved vertical-cavity surface-emitting laser (VCSEL) performance[9] but these techniques have not been used in edge-emitters prior to this work. In fact, since the composition grades are not constrained by optical resonance conditions, edge-emitters present a much larger design space for use of graded interfaces allowing for greater reductions in barrier height. Using one-dimensional simulations of the heterojunction band structure, the potential barrier height of oxidation-layer interfaces within BOW lasers has been reduced to less than 15 meV for both the p-type and n-type high-Al-content layers. This low barrier is a consequence of using fully bi-parabolic graded interfaces and is smaller than barriers typically built into uni-parabolic graded VCSEL interfaces.

Lasers were fabricated using metal-organic chemical-vapor deposition of (Al,Ga)As on n-type-doped GaAs substrates. Waveguide material is 60% Al with 175 nm thick grade between 60% and 30% Al forming a graded-index separate confinement heterostructure (GRINSCH) waveguide around a 10 nm GaAs single quantum well (SQW) active region. 40-nm-thick 98%-Al AlGaAs layers for selective oxidation are located on both sides of the graded waveguide. Mesas between 20 and 40 μm wide were etched through to the substrate and steam oxidized at 420° C to create oxide layers with apertures between 2.3 μm and 25 μm in width. SiO_2 was deposited between the mesas to insulate the n-type material from the top ohmic contact and the entire mesa surface was used to form the upper p-type ohmic contact with Pt/Ti/Pt/Au metalization. After completion of the p-side, the wafer was thinned, Pd/Ge/Au ohmic contact metalization applied and the entire structure heat-treated at 175°C. Fig. (1.2) is a SEM cross section image of a completed laser. The gap between the darkest gray laterally oxidized regions, corresponding to the optical waveguide, is clearly seen. The upper and lower oxide apertures are slightly different in width due to a 14% difference in oxidation rate of the n- and p-type AlGaAs oxidation layers in this configuration.

Lasers were tested p-side up without heat sinking or facet coatings using 1 μs pulses at 10 kHz repetition rate. Fig. (1.3) shows pulsed light-versus-current data for 300-μm-long BOW lasers with 4-μm-wide waveguide apertures. The 300 μm laser has a threshold current, I_{th}, of <6 mA and a threshold density, J_{th}, of 486 A/cm^2. The slope efficiency is constant at 1.15 W/A (assuming equal power from rear facet) for all tested currents. Longer, 600-μm lasers (Fig. 1.4) has I_{th} = 8.7 mA, J_{th} = 307 A/cm^2, and slope efficiency of 1.48 W/A. At the operating wavelength these devices have external differential quantum efficiencies of 0.79 (short laser) and >0.95 (long laser). Wall-plug efficiency of the long laser peaks at 40%.

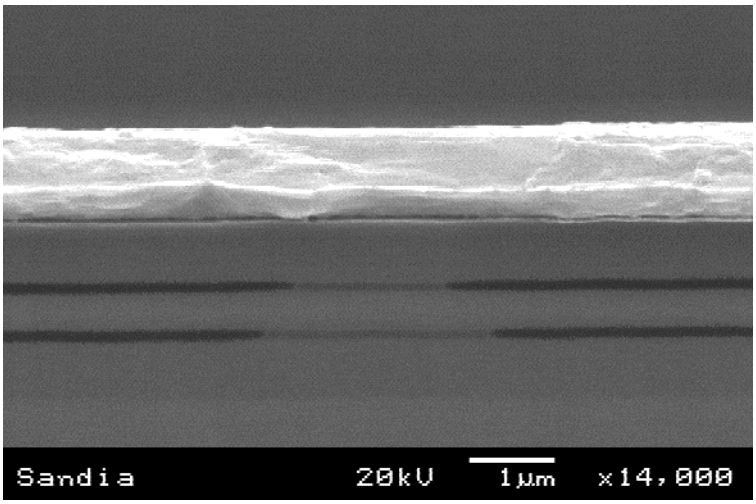

Figure 1.2: Scanning electron micrograph of completed BOW laser. Selectively oxidized regions are the dark lines extending in from the sides of the image.

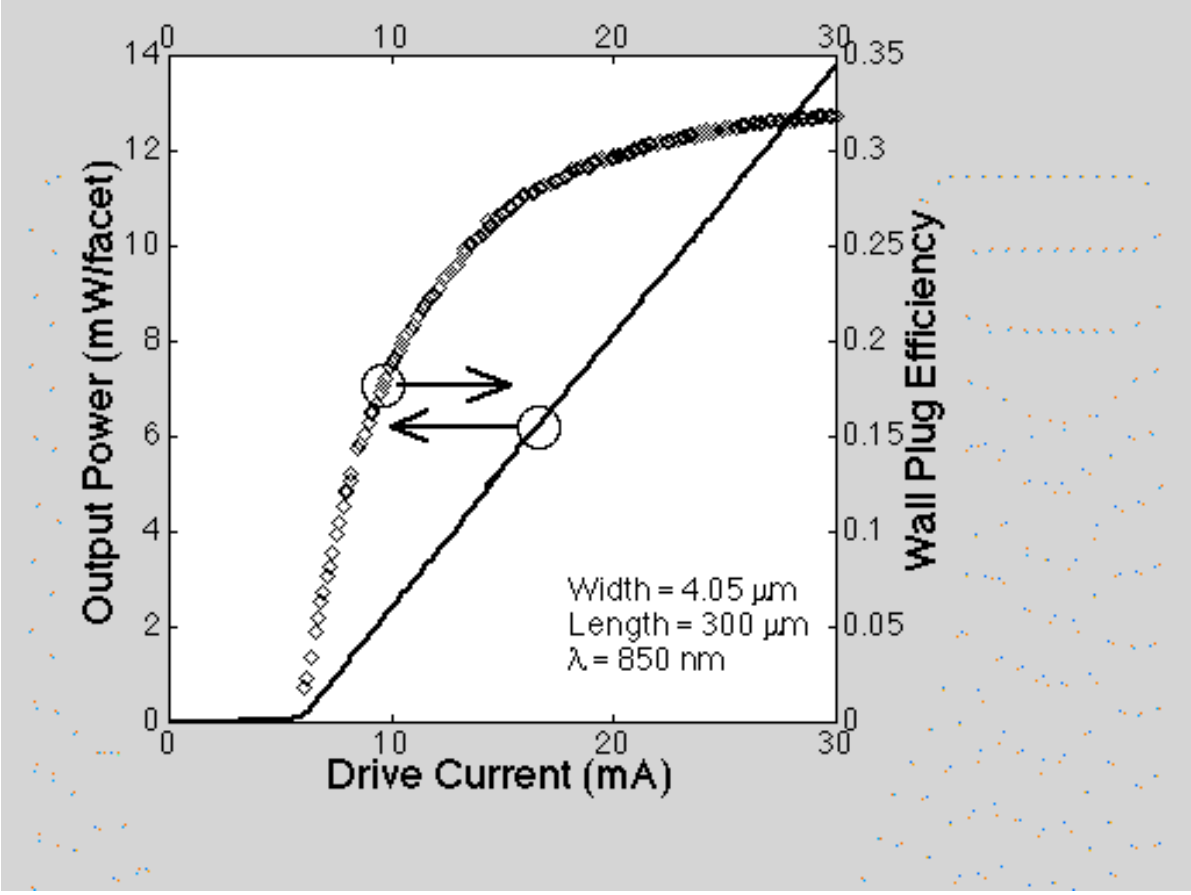

Figure 1.3: Light output (solid line) and wall-plug efficiency (diamonds) versus injection current of a 300-µm-long by 4 µm wide BOW laser.

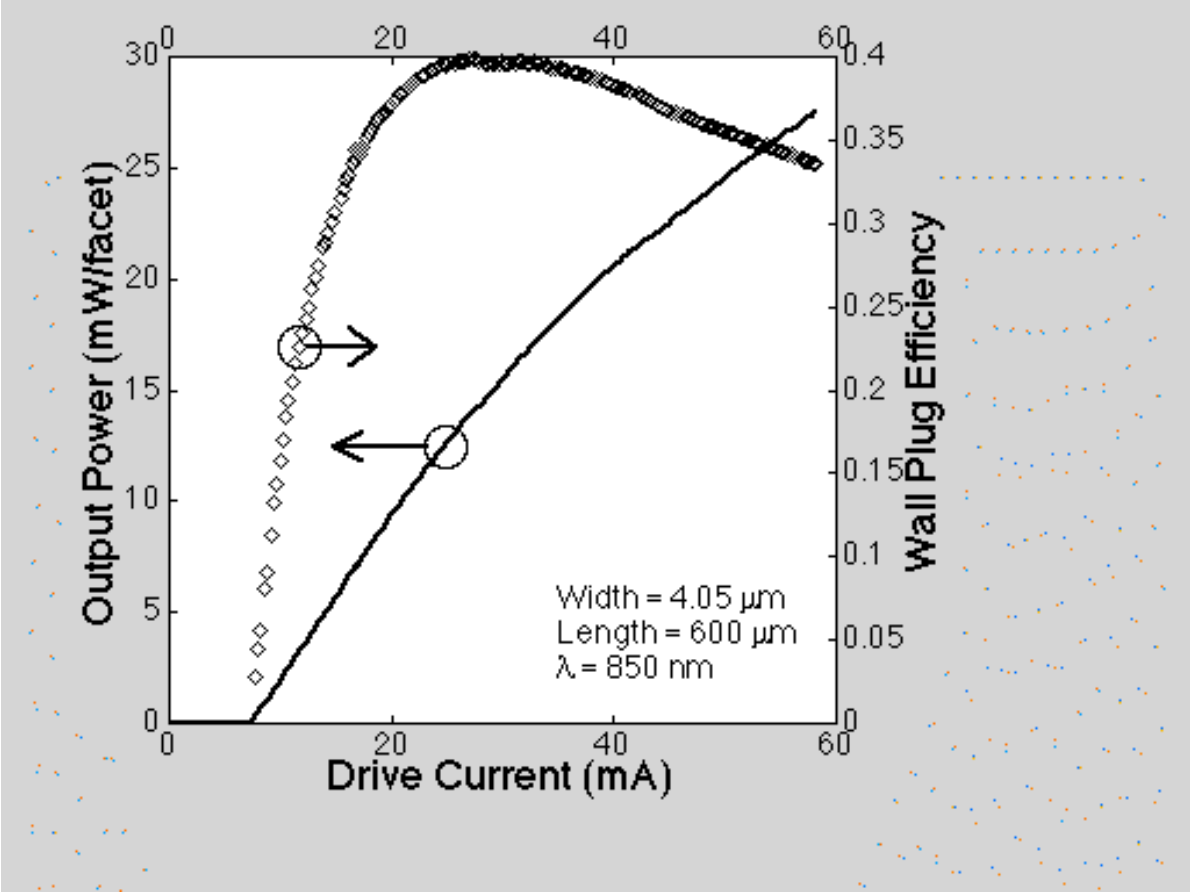

Figure 1.4: Light output (solid line) and wall-plug efficiency (diamonds) versus injection current of a 600-µm-long by 4 µm wide BOW laser.

Wall-plug efficiency of both lasers is limited by the ~2.3 V threshold voltage. Examination of current-voltage characteristics suggests that this high threshold voltage is due to excessive series resistance, possibly due to high specific contact resistance.

Ensemble average data for threshold current and external differential quantum efficiency from 70 tested lasers is presented in Fig. 1.5. Threshold current of 300-µm-long lasers decreases monotonically with width suggesting that narrower lasers with lower threshold are possible. The longest (900 µm) lasers are more sensitive to internal loss and show a minimum threshold current at 4 µm width. External differential quantum efficiency is only weakly varying with laser width (except for the 25-µm-wide devices where filamentation may dominate) indicating that losses attributable to the BOW waveguide are quite low even for very narrow guides with significant overlap of the optical mode and the oxidized material. Calculation of overall internal losses from the measured data for laser widths between 2.3 µm and 12 µm gives losses between 2.9 cm^{-1} and 4.4 cm^{-1} including all scattering and self-absorption effects. Little, if any, correlation with width exists in the loss values suggesting that, within the uncertainty of the experiment, narrow BOW lasers do not introduce additional internal waveguide loss due to scattering or absorption by the oxide or oxide interfaces.

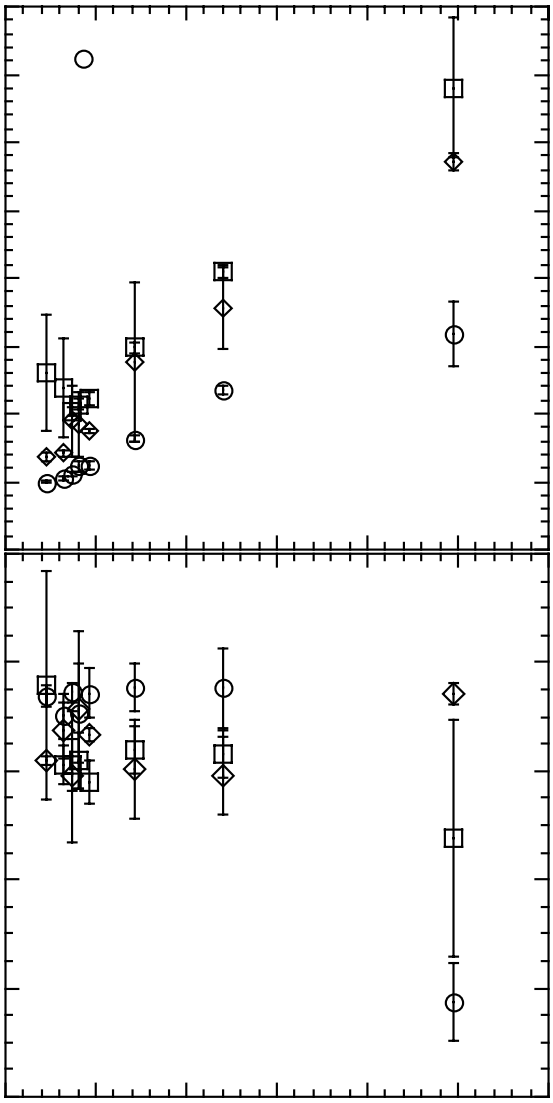

Figure 1.5: Threshold current and external differential quantum efficiency of BOW lasers as a function of laser width.

In summary, we have demonstrated a highly efficient BOW laser using dual selectively-oxidized AlGaAs layers to form both the optical waveguide and the current confinement regions. Optimization of the waveguide design, oxide layer placement, and bi-parabolic grading of the heterointerfaces on both sides of the AlGaAs layers for oxidation has yielded 95% external differential quantum efficiency and 40% wall-plug efficiency from a laser that is very simple to fabricate and does not require epitaxial regrowth of any kind. Further improvments in wall-plug efficiency and threshold are anticipated through the use of narrower waveguides, facet coating, and reduced threshold voltage.

References:

[1] K. Choquette, K. Geib, C. Ashby, R. Twesten, O. Blum, H. Hou, D. Follstaedt, B. Hammons, D. Mathes and R. Hull,"Advances in selective wet oxidation of AlGaAs alloys," IEEE J. Selected Topics in Quantum Electronics, vol. 3, pp. 916-926, 1997.

[2] J. M. Dallesasse, J. N. Holonyak, A. Sugg, T. Richard and N. El-Zein,"Hydrolyzation oxidation of $Al_xGa_{1-x}As$-AlAs-GaAs quantum well heterostructures and superlattices," Appl. Phys. Lett., vol. 57, pp. 2844-2846, 1990.

[3] J. Dallesasse and J. N. Holonyak,"Native-oxide stripe geometry $Al_xGa_{1-x}As$-GaAs quantum-well heterostructure lasers," Appl. Phys. Lett., vol. 58, pp. 394-396, 1991.

[4] Y. Cheng, G. Yang, M. MacDougal and P. Dapkus,"Low-threshold native-oxide confined narrow-stripe folded-cavity surface-emitting InGaAs-GaAs lasers," IEEE Phot. Technol. Lett., vol. 7, pp. 1391-1393, 1995.

[5] W.-J. Choi and P. D. Dapkus,"Self-aligned AlAs oxide-current-aperature buried-heterostructure ridge waveguide InGaAs single-quantum-well diode laser," IEEE Phot. Technol. Lett., vol. 11, pp. 773-775, 1999.

[6] S. A. Maranowski, A. R. Sugg, E. I. Chen and N. Holonyak,"Native oxide top- and bottom-confined narrow stripe p-n $Al_yGa_{1-y}As$-GaAs-$In_xGa_{1-x}As$ quantum well heterostructure laser," Appl. Phys. Lett., vol. 63, pp. 1660-1662, 1993.

[7] J. Heerlein, M. Grabherr, R. Jager and P. Unger,"Single-mode AlGaAs-GaAs lasers using lateral confinement by native-oxide layers," IEEE Phot. Technol. Lett., vol. 10, pp. 498-500, 1998.

[8] J. Heerlein, S. Gruber, M. Grabherr, R. Jager and P. Unger,"Highly efficient laterally oxidized λ=950 nm InGaAs-AlGaAs single mode lasers," IEEE J. of Selected Topics in Quantum Electronics, vol. 5, pp. 701-706, 1999.

[9] K. L. Lear and R. P. Schneider,"Uniparabolic mirror grading for vertical cavity surface emitting lasers," Appl. Phys. Lett., vol. 68, pp. 605-607, 1996.

Resonant Reflector Lasers for Photonic Integration

The resonantly-enhanced-mirror (REM) laser uses an air gap to control optical feedback and coupling efficiency to an external waveguide (Fig. 2.1). Low contrast waveguides give relatively large mode cross-sections and low diffraction loss at the laser-waveguide coupling gap. Preliminary models indicate that 60% modal reflectivity and 2 dB coupling loss can be achieved using this approach.

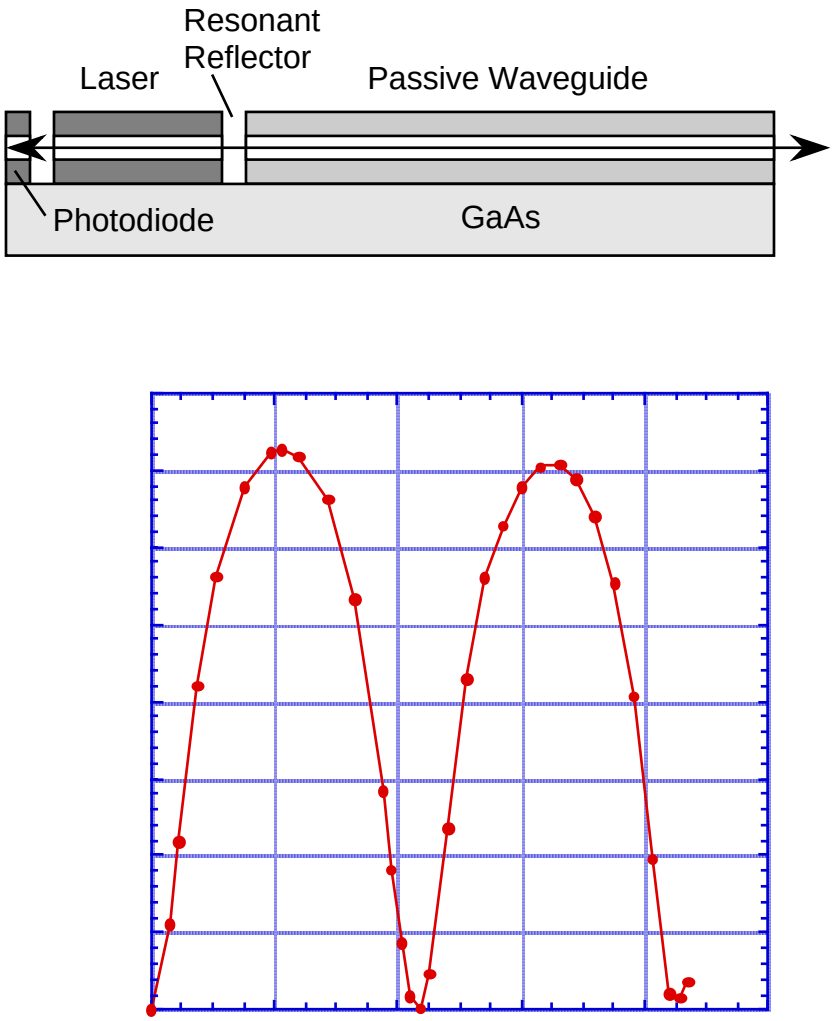

Figure 2.1: Schematic (top) of resonantly enhanced mirror laser showing air gap for feedback and waveguide coupling. Simulation (bottom) of modal reflectivity versus air gap.

Resonant-reflector lasers made good progress during the shortened, two-year, duration of the program. We have demonstrated the merits of using a single air gap at the etched-facet endface of edge-emitting diode lasers to enhance the effective facet reflectivity significantly, a development relevant to passive waveguides coupled to etched-facet active devices which require this index discontinuity for cavity feedback. Our initial results for a deep-rib MQW GRINSCH laser are shown in Figure 2.2 which gives the pulsed threshold current versus nominal gap width relative to doubly-etched devices (with no external reflection) and doubly cleaved devices. This Figure also shows an experimental fit of the analytic variation in Ith expected by varying the gap width (which varies the phase of the feedback from the external reflector). Detailed calculations of the theoretical facet reflectance were previously made and are shown in Figure 2.3 for comparison. While these early results indicate that our etched-facet reflectivity is lower than the cleaved value (calc. R = 0.306), the additional reflection interface clearly shows an enhanced effective reflectivity that reduces I_{th} for an appropriately chosen gap width.

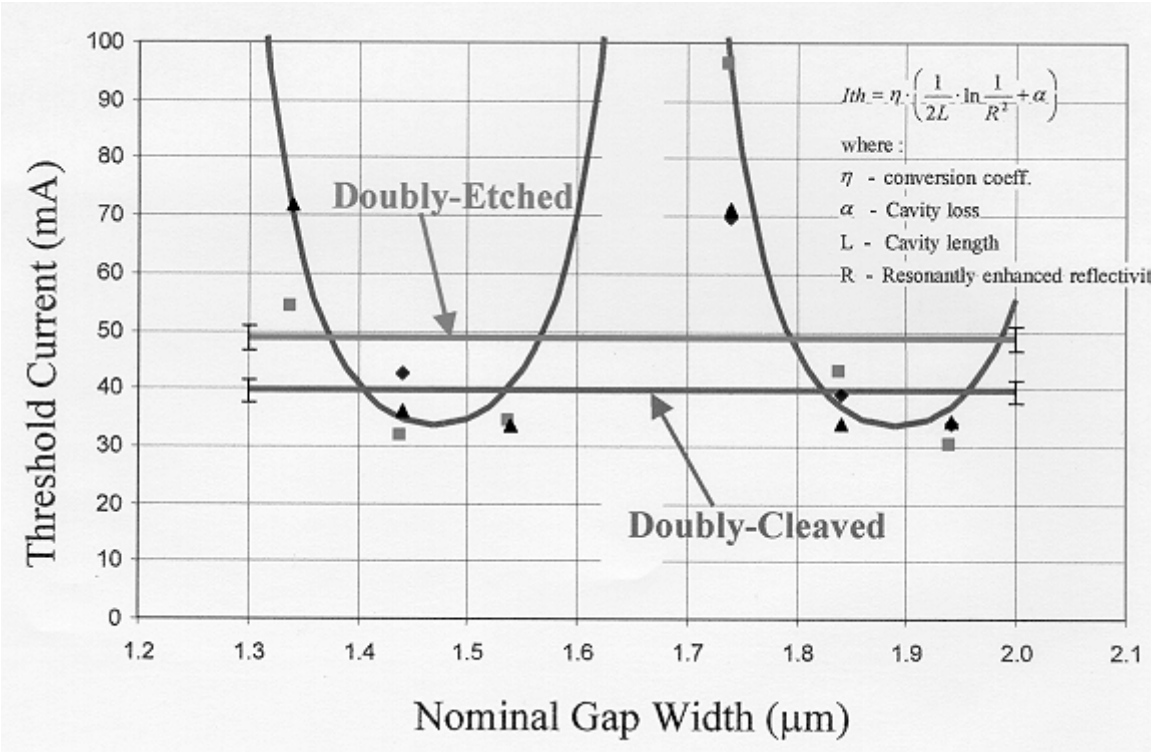

Figure 2.2: Laser threshold current versus gap width for resonantly enhanced reflector lasers. Threshold dips below that of conventional lasers (horizontal lines) when the gap width generates constructive interference.

Recent SQW GRINSCH lasers show much lower I_{th} than MQW devices. Our best L-I-V terminal characteristics for resonantly-enhanced etched-facet edge-emitting lasers are a substantial improvement over the previous year's results. Adjacent devices which were doubly-etched or doubly-cleaved show I_{th} in the 15-16 mA range, indicating a 5mA improvement in oscillation threshold due to resonant enhancement of the facet reflectivity. Results for I_{th} versus cavity length for this laser design are summarized in Figure 2.4.

Analysis of the 5-micron-wide laser fitting equations for I_{th} as a function of cavity parameters (such as R_{eff} and L) indicate an effective facet reflectance of about R_{eff} (enhanced) = 0.51 relative to the assumed reflectance of R_{eff} = 0.31 for both the doubly-etched and doubly-cleaved devices. The difference in slopes between the 5 μm and 3 μm data suggests a substantially degraded facet reflectance (est. R_{eff} ~ 0.057) for doubly-etched 3-μm-wide devices compared to 5-μm-wide devices. This is probably due to rounding of the rib at the endface.

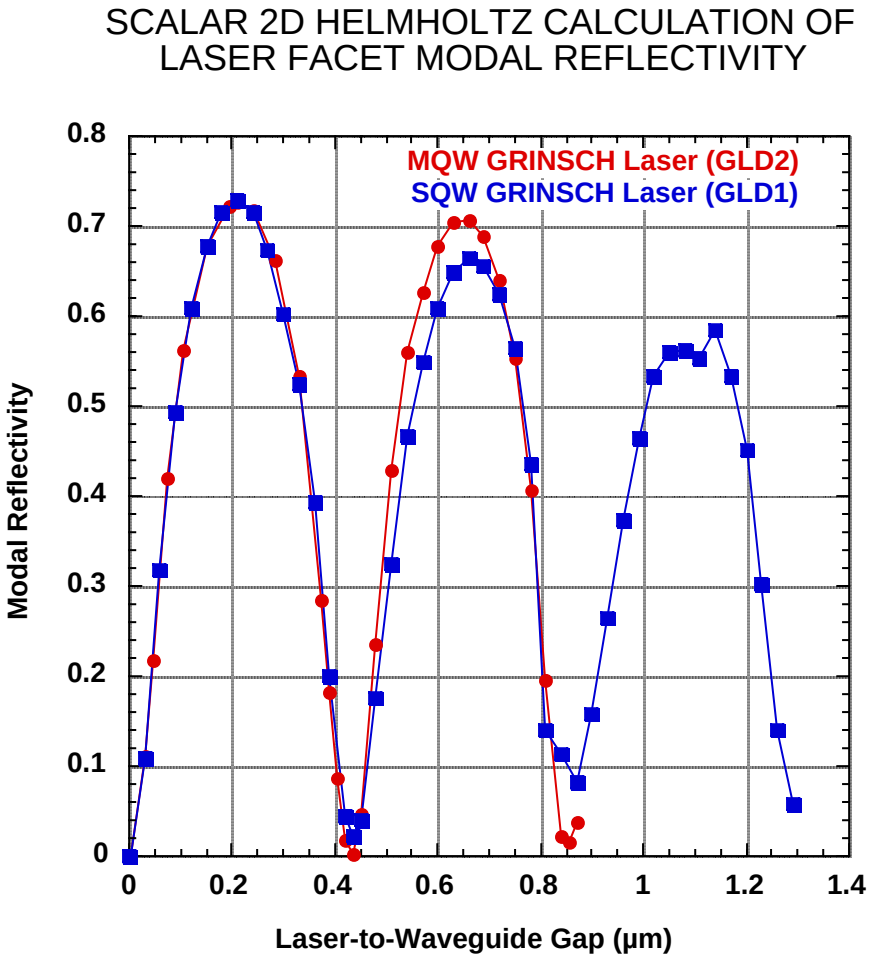

Figure 2.3: Simulation of resonant facet reflectivity.

Reverse-biasing a high-quality diode laser is expected to give very good L-I-V characteristics well suited for many applications requiring integrated diode lasers and waveguide photodetectors. Lasers developed during the last year show low reverse saturation leakage (or dark) current of less than 30 pA independent of bias (showing low shunt parasitics) and high breakdown voltage. Accurate measurements of absolute responsivity of devices in reverse bias have been very difficult due to uncertainities in coupling efficiency (est. 3dB uncertainty) and is currently being studied. With this

substantial uncertainty, we believe the internal responsivity of our diode lasers lies in the 0.3-0.6A/W range.

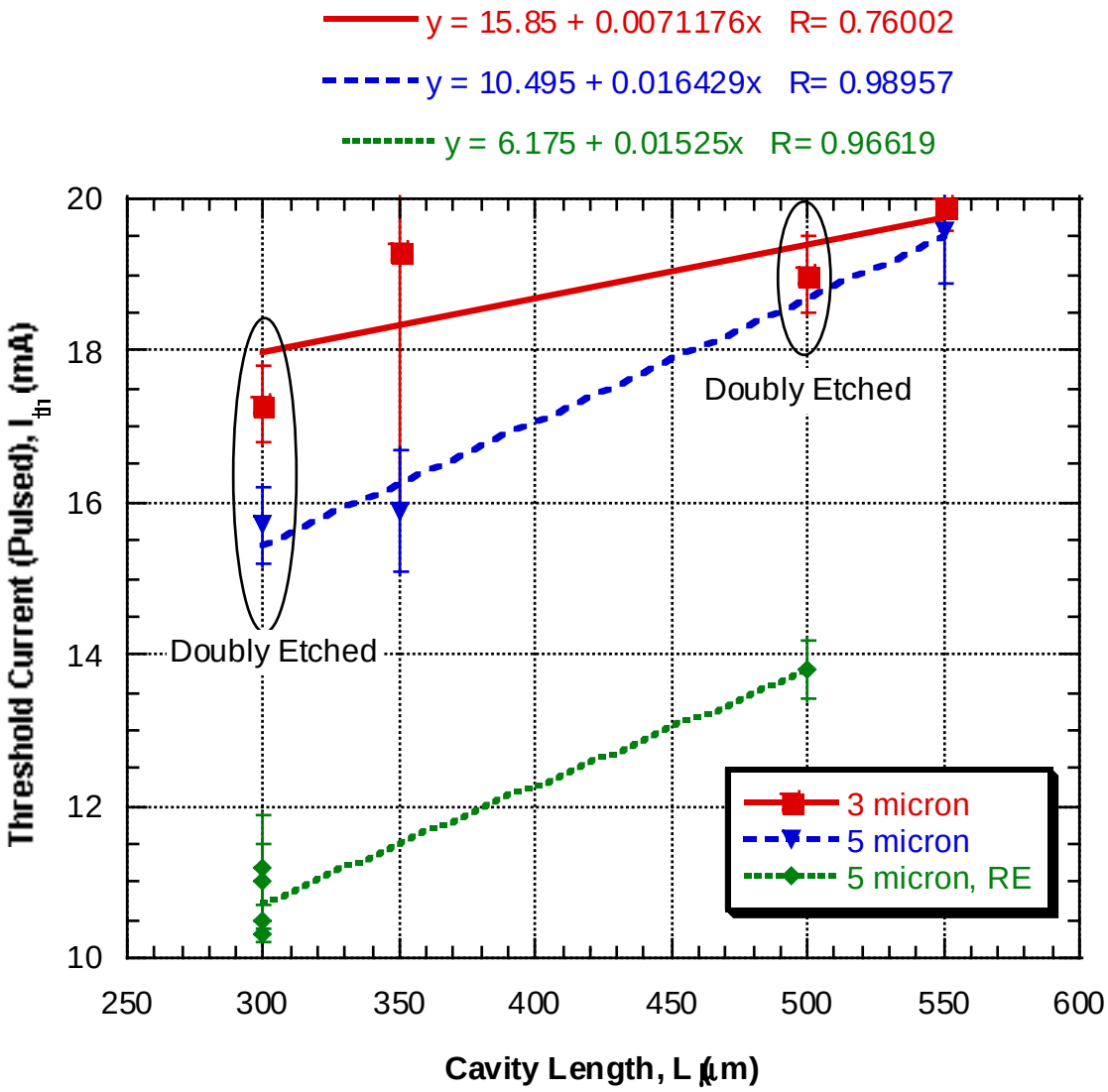

Figure 2.4: Threshold current plotted versus cavity length in order to determine facet reflectivity. Strong reduction of threshold for resonantly enhanced (RE) lasers is seen.

Waveguiding with Photonic Lattices

In this paper, a waveguide-coupled 2D photonic crystal slab is successfully fabricated from a GaAs/Al2O3 material system. The 2D crystal is shown to have a strong 2D photonic band gap at $\lambda \sim 1.5$ μm. Light is attenuated to less than 10^{-3} in the band gap for a nine-period 2D crystal, the strongest ever reported for any 2D crystal in optical λ. Moreover, for the first time, it is shown that the 2D slab structure can indeed confine light fully in z-direction.

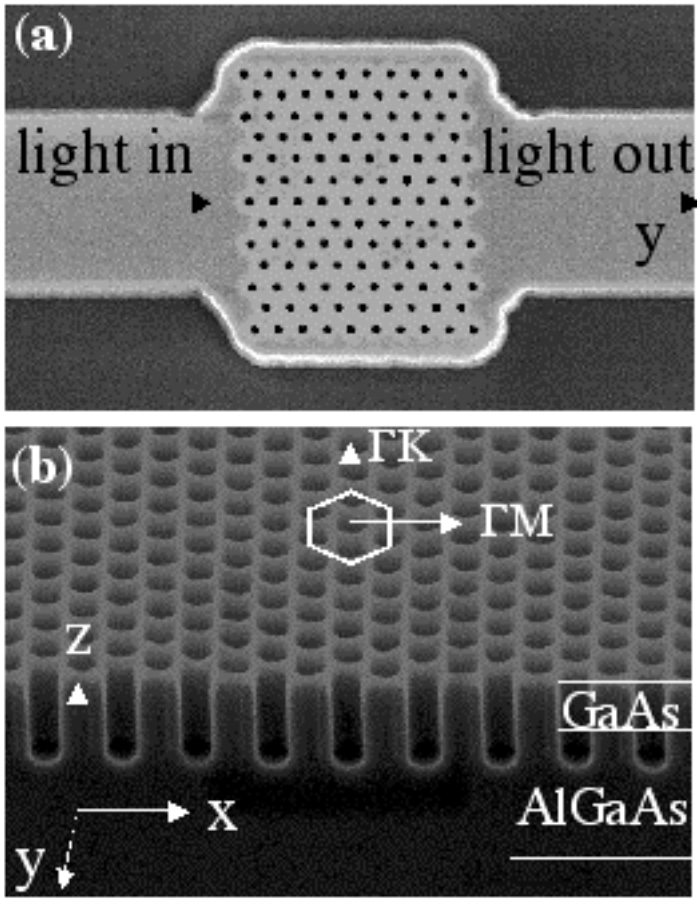

Figure 3.1: Electron microscope images of 2D photonic crystal slab. (a) Top view showing an input ridge waveguide, a nine period 2D hole array and an output waveguide. The holes are arranged in a triangular array, and the waveguides are used to facilitate light coupling. The 2D hole array section is a few rows wider than the waveguide to reduce light leakage around the side edges of the photonic crystal slab. (b) A side view of the etched cylindrical holes, which have an etched depth of ~0.5 μm and side walls straight to within 5°. Nanometer-scale fabrication of 2D holes is done using a combination of electron-beam lithography and reactive-ion-beam etching processes. The major crystal symmetry directions, Γ-K and Γ-M, are also shown. Scale bar, 1 μm.

The sample was grown on (001) GaAs substrate by MOCVD and consists of a 1μm thick $Al_{0.9}Ga_{0.1}As$ layer and a thin slab of GaAs layer. The 2D photonic crystal is fabricated by etching 2D cylindrical holes through the GaAs slab. The holes are arranged in a triangular array fashion with lattice constant a and hole diameter d (= 0.6 *a*). Three sets of samples were fabricated with a = 400, 430 and 460 nm respectively. A conventional ridge waveguide is then etched through the $Al_{0.9}Ga_{0.1}As$ layer. This completes the construction of an integrated waveguide-coupled 2D photonic crystal sample. In Fig. 3.1(a), an image of a nine period 2D photonic crystal slab is shown. The 2D hole array section is a few rows wider than the waveguide. This is done because the fabricated hole size tends to be more uniform at the middle rows and becomes less controllable near the edges. As a final step of the fabrication, the $Al_{0.9}Ga_{0.1}As$ layer is wet oxidized into Al_xO_y (n ~ 1.60) for two purposes. In the ridge waveguide region, it acts as the cladding layer for guiding the input and output light. In the 2D hole array region, it helps confining light in the 2D plane and eliminates light leakage into either air or the GaAs substrate. The ridge waveguide also serves as the interface between input/output optics and the 2D photonic crystal slab.

Nano-meter scale fabrication of 2D holes is accomplished using a combination of electron-beam lithography and reactive-ion-beam-etching (RIBE) processes. Before patterning, a 200 nm thick SiO_2 layer and a 400 nm thick PMMA photo-resist were deposited on top of the GaAs slab. The PMMA serves as a mask for the direct-write electron-beam lithography process. The SiO_2 layer serves as a mask for etching GaAs/ $Al_{0.9}Ga_{0.1}As$ layers, using a chlorine-based RIBE process. The RIBE technique allows for etching of GaAs / $Al_{0.9}Ga_{0.1}As$ materials with a straight and smooth side-wall. In Fig. 3.1(b), a side view image of a fabricated sample is shown. The depth of holes is ~0.5 μm and indeed the side-walls are straight.

In Fig. 3.2(a), energy dispersion of a 2D photonic crystal slab, computed using a full 3D calculation, is shown. The 2D slab has a thickness of $t = 0.5\ a$ and is so chosen to maximize the photonic band gap. The frequency ω is expressed in a reduced unit, (a/λ) and the wavevector plotted along crystal symmetry axis, Γ, M and X. The shaded region represents the light-cone and the connected dots are guided modes. Light-cone is a new feature that follows from a full 3D calculation and does not occur from a pure 2D band structure calculation. Photonic states within light-cone extend into regions outside the slab and are leaky. These are the undesirable radiation modes. The slope of light-cone boundary is determined by the index of the underlining Al_xO_y layer (n ~ 1.6).

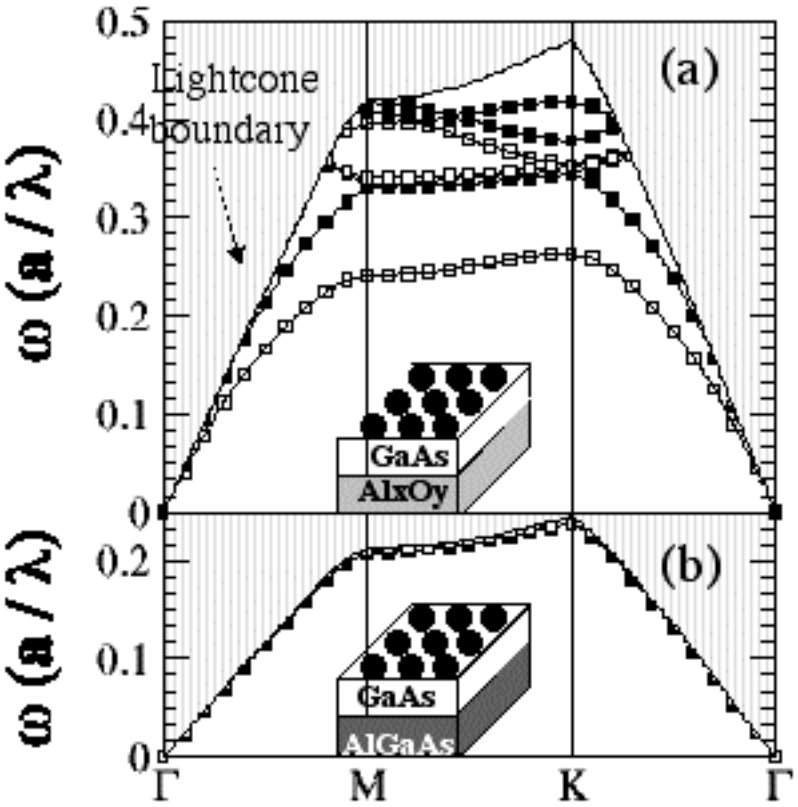

Figure 3.2: Computed dispersion of 2D photonic crystal slab structures. Here, ω is expressed in units of (a/λ), and k is plotted along symmetry directions, Γ, M(π/a) and K($1.15\pi/a$). (a) The bottom cladding layer is Al_xO_y, with a refractive index n~1.5. See text for discussion of light cone boundary and the shaded area. (b) The bottom cladding layer is $Al_{0.9}Ga_{0.1}As$ (n=2.9).

The guided modes, on the contrary, are localized vertically to within the 2D slab. This confinement is analogous to total-internal-reflection and is due to a large index contrast between GaAs (n=3.4) and AlO_x layers. Guided modes are classified into TE-like (solid dots) and TM-like (open squares) states, according to whether they are even or odd with respect to reflections through the 2D plane [9]. For a perfectly symmetrical 2D slab, TE- and TM-modes are de-coupled and mutually non-interacting. As shown in Fig. 3.2(a), a large fundamental TE band gap exists, ranging from ω=0.25 to ω=0.33. There is also a higher order TM-gap at ω =0.35 to ω =0.385. Operating within the guided modes, light propagates freely in the 2D plane. In the band gap regime, on the other hand, light is strongly confined in the 2D plane and at the same time is index-guided vertically. It is in this sense that light can be fully confined using a 2D photonic crystal slab.

For comparison purpose, dispersion for an un-oxidized 2D photonic crystal slab is also shown in Fig. 3.2 (b). In this case, the slope of light-cone, c/n, is set by the index of $Al_{0.9}Ga_{0.1}As$ layer, n = 2.9. A higher n implies a lower light-cone boundary for the un-oxidized 2D slab structure. Consequently, only the lowest TE-like and TM-like bands exit and no photonic band gap is expected. The use of low index AlO_x layer in our 2D slab

structure design is simple and yet essential for obtaining 2D guided modes and fully confined gaps.

To probe the intrinsic optical properties of a 2D photonic crystal slab, transmission measurements were carried out. Three diode laser modulates were used as light source. The laser output has a well-defined Gaussian profile, and is tunable over a wide wavelength range, from λ = 1290 to 1350 nm, λ = 1525 to 1595 nm and 1625 to 1680 nm. This tuning range allows us to simultaneously probe band gaps, band edges and guided modes of the 2D crystal dispersion in optical λ. For polarization study, a polarization rotator was used to produce pure TE and TM input light. To couple laser light into the ridge waveguide, an aspheric lens with a high nemerical aperature (NA=0.4) were used. An identical lens is also used to collect the transmitted light. The collected light is then split and fed into a calibrated InGaAs photo-detector and an infrared (IR) camera respectively. For precise optical alignment, sample and lenses are mounted to a 5-axis moving stage, which has a movement precision of better than 50 nm.

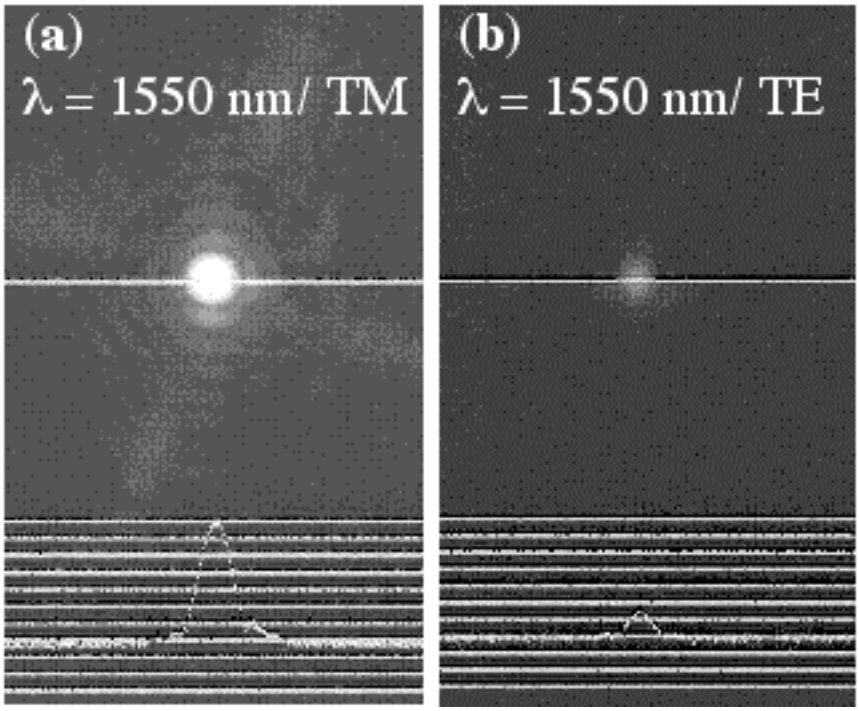

Figure 3.3: Infrared images of the transmitted laser light, and their corresponding modal profiles at l=1550 nm. The input laser light is coupled into and out of a ridge waveguide using a pair of aspheric lenses with a high numerical aperture (NA = 0.40. An infrared camera is used to image the laser output. (a) The image of TM transmitted light is brighter as it belongs to a guided mode. (b) The TE transmitted light is much weaker and is in the photonic bandgap spectral regime. Both TM and TE modal profiles are gaussian-like. The horizontal lines are guides to the eye.

To obtain a reliable transmittance data, modal profile of the transmitted light must be carefully examined. In our experimental configuration, transmitted signal is a combined

effects of light coupling from (1) the input waveguide mode into (2) the photonic crystal state and then back to (3) the output waveguide mode. If laser light is well focused into the input waveguide and the 2D crystal does not randomly scatter light, output signal is a well-defined Gaussian-shape waveguide mode. On the other hand, if the focus is off and laser light is coupled, instead, into the undesired air mode or substrate leaky mode, output signal is typically broad and scattered in shape. An infrared imaging camera at the output end is a useful tool for checking modal profile. In Fig. 3.3(a), an infrared image of a TM light of λ=1550 nm transmitted through a nine-period 2D crystal sample (a=460 nm) is shown. The mode is bright and well defined. Its intensity profile, shown at the bottom as a dashed line, follows a Gaussian-shape. The same measurement is repeated with TE polarized light and the resulting image shown in Fig. 3.3(b). The image is not as bright, but its profile remains a Gaussian-shape. The observed Gaussian profile suggests that the output signal is a true measure of waveguide-photonic crystal interaction. Also, the much weaker TE intensity suggests the existence of a TE gap at λ = 1550 nm.

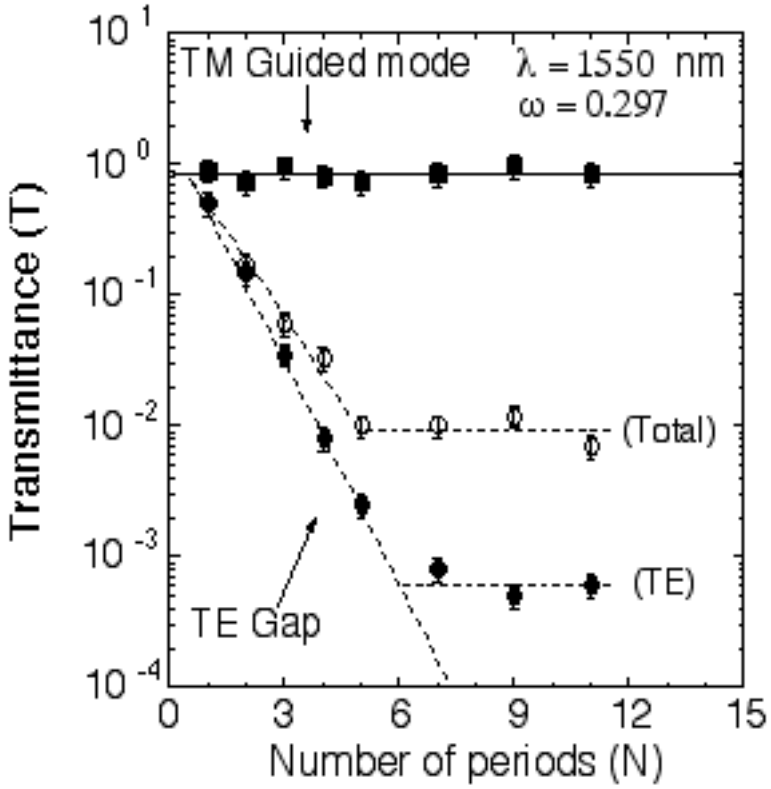

Figure 3.4: Absolute transmittance (T) at ω=0.297 taken from a series of samples with different number of periods (N). The transmittance for TM input is shown as filled squares. For TE input, transmitted light contains both TE and TM components. Both the TE (solid circles) and total (open circles) transmitted light attenuates exponentially as a function of N. See text for details.

To find absolute transmittance of a 2D crystal, a reference transmission is taken from an identical waveguide with no 2D crystal built in the middle section. By rationing transmission

signals, taken with and without a 2D crystal, absolute transmittance is obtained. This normalization procedure eliminates uncertainties associated with reflection at waveguide-crystal interface and free space-to-waveguide coupling efficiency.

In Fig. 3.4, the TM absolute transmittance vs number-of-period (N) of a 2D hole array (a = 460 nm) is plotted as solid squares. The laser wavelength is λ=1550 nm, and its corresponding reduced frequency ω (= a/λ) is 0.297. The transmittance is high, (85 ± 10)%, and is also independent of N. The high transmittance shows that TM light is well guided within the 2D photonic crystal slab. Indeed, at ω = 0.297, our earlier band structure calculation predicts a guided TM mode along Γ-K. This data also suggests that out-of-plane scattering due to fabrication imperfection is not important. For TE input at ω = 0.297, light is strongly attenuated and, quite surprisingly, is also slowly been converted to TM polarization. In Fig. 3.4, the total and TE transmitted light is plotted as open and solid dots, respectively. Only TE transmitted light will be discussed here and the polarization conversion issue will be addressed later. The TE transmittance drops exponentially from 50% at N=1, to ~ 0.2 % at N=5, and eventually saturates at ~ 6 x 10^{-4}, which is the noise level of our detector. The observed exponential dependence shown that, at ω = 0.297, TE mode is in the photonic band gap regime. This result agrees with the prediction presented in Fig. 3.2(a). The attenuation power of this photonic band gap is very strong. Light attenuates a factor of 10, for every two-periods it traverses in the crystal, i.e. ~ 5dB/ per period.

To explore the full dispersion of a 2D photonic crystal slab, nine experimental data sets were taken covering frequency ω from 0.24 to 0.36. This task is accomplished by scanning three laser modulates through three sets of 2D crystals with a = 400 nm (red dots), 430 nm (green dots) and 460 nm (blue dots), respectively. In Fig. 3.5(a), the measured TE transmission spectrum is plotted in a semi-log scale. The photonic band gap formation is clearly seen. A theoretical curve (the solid line) for the same 2D crystal slab is also shown. The agreement between theory and experiment is good. The slightly larger observed band gap, ~8 %, may be due to small uncertainties in hole size and lattice constant. In the band gap regime, transmittance minimum as low as T ~ 2 x 10^{-4} is observed at $\omega \sim 0.27$. This is the strongest attenuation ever reported for any 2D photonic crystals operating in the optical wavelengths. The upper and lower TE band edges occur at $\omega_1 \sim 0.35$ and $\omega_2 \sim 0.25$, respectively. The gap-to-midgap ratio is large, $(\omega_1 - \omega_2)/(\omega_1 + \omega_2) = 33\%$. Within this band gap, light is truly confined in all three dimensions, i.e. strongly confined in the 2D plane and index guided vertically.

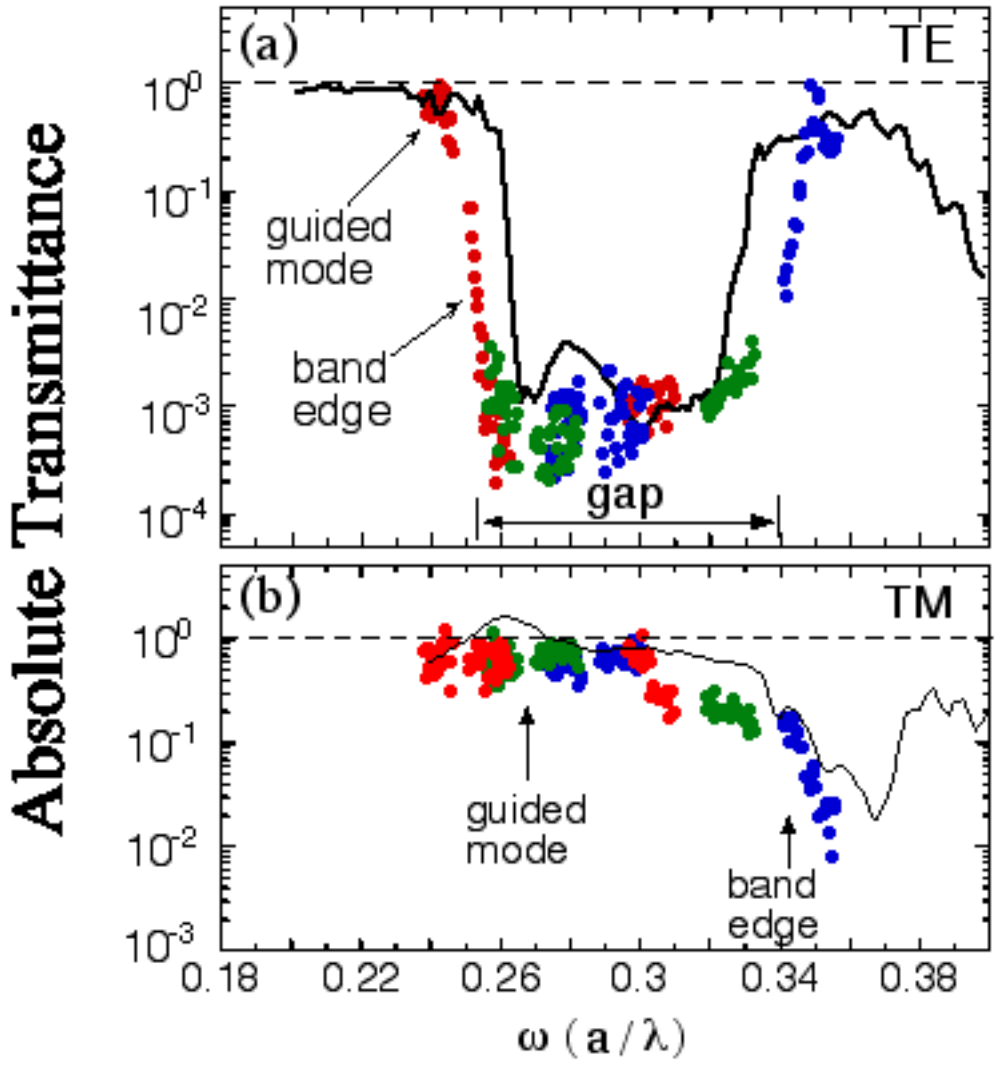

Figure 3.5: Absolute transmittance (T) as a function of ω (=*a*/λ) from 0.18 to 0.40. (a) The TE transmittance spectrum covers the guided mode (~100% transmission at ω=0.24), band edge, and band gap regions. The solid line is a theoretical curve. Here, ω is varied by tuning λ through three samples with different *a*; 400 nm (red dots), 430 nm (green dots) and 460 nm(blue dots), respectively. (b) The transmittance for TM light. The solid line is a theoretical curve.

In Fig. 3.5(b), the measured TM transmission spectrum is also plotted, along with a theoretical curve (solid line). In the guided mode regime, ω = 0.24–0.30, transmittance is close to 80-100% and light is fully guided in the 2D plane. The position and magnitude of the first TM gap at ω = 0.35–0.38 also agrees well with the computed value.

The polarization conversion mentioned in Fig. 3.4 may be attributed to symmetry breaking in the 2D slab structure. In our sample, the upper cladding is a thin 0.05 μm SiO_2 layer, whereas the lower cladding is a thick 1μm Al_xO_y layer. This asymmetry [11] introduces a weak coupling between TE-like and TM-like mode. At ω = 0.297, while TE

light is attenuated due to TE gap, TM light is free to propagates. For small N (<3) in Fig. 3.4, TE light dominates and its intensity close to the total transmitted light. For $3 < N < 5$, the converted TM intensity increases yet TE light continues to drop, leading to a large difference between TE and the total transmitted light. For $N > 5$, TM polarization dominates the total transmitted light and its intensity remains a constant as it is a guided mode. This TE-to-TM conversion process contributes to light leakage and will limit the reflecting efficiency of a TE gap. However, it is not an intrinsic problem. Through a symmetrical slab structure design, such a leak can be eliminated.

This work realizes a new class of 2D photonic crystal structure that offers light guiding and full light confinement in the optical λ. These important optical properties are obtained through the use of a optimally-designed thin 2D slab and the addition of a low index underlying AlO_y layer. The fabrication simplicity of the 2D slab structure makes it an attractive alternative/complimentary to its 3D counter part. This demonstration set a new framework for 2D crystal structure and will draw impacts to a whole class of planar-photonic-circuits applications. Examples are low loss in-plane wave-guides/bends, high reflectivity in-plane mirrors for laser and filter applications, and non-linear photonic crystal prisms for wavelength division multiplexer/de-multiplaxer applications.

References

[1] J.D. Joannopoulos, R.D. Meade and J.N. Winn, Photonic Crystals, (Princeton, New York, 1995).

[2] C.M. Soukoulis, Photonic Band Gap Materials: The "Semiconductors" of the Future, Physica Scripta, T66, 146-150 (1996).

[3] J.D. Joannopoulos, P.R. Villeneuve, S. Fan, Photonic Crystals: putting a new twist on light, Nature, 386, 143-149 (1997).

[4] S.Y. Lin *et al.*, A three-dimensional photonic crystal operating at infrared wavelengths, Nature, 394 251-253 (1998).

[5] C.C. Cheng, V. Arbet-Engels, A. Scherer and E. Yablonovitch, Nanofabricated three dimensional photonic crystals operating at optical wavelengths, Physica, Scripta, T68, 17 (1996).

[6] S.Y. Lin, E. Chow, V. Hietala, P.R. Villeneuve, J.D. Joannopoulos, Experimental Demonstration of Guiding and Bending of Electromagetic Waves in a Photonic Crystal, Science 282, 274-276, 1998.

[7] W.M. Robertson *et al.*, Measurement of Photonic Band Structure in a Two-Dimensional Periodic Dielectric Array, Phys. Rev. Lett. 68 2023-2026 (1992).

[8] Thomas F. Krauss, Richard M. De La Rue, and Stuart Brand, Two-dimensional photonic bandgap structures operating at near-infrared wavelengths, Nature 383 699-701 (1996).

[9] D. Labilloy *et al.*, Quantitative Measurement of transmission, reflection, and diffraction of Two-Dimensional Photonic Band Gap Structures at Near-Infrared Wavelengths, Phys. Rev. Lett. 79, 4147 (1997).

[10] D. Labilloy *et al.*, Finely resolved transmission spectra and band structure of two dimensional photonic crystals using emission from InAs quantum dots.

[11] S.G. Johnson, S. Fan, P.R. Villeneuve, J.D. Joannopoulos, Guided modes in photonic crystal slabs, Phys. Rev. B 60 5751-5758 (1999).

Low-Loss Waveguides for Active-Passive Integration using Impurity-Free Vacancy Diffusion

Impurity-free vacancy diffusion[2] is a method by which an SQW or MQW waveguide may be made less absorptive at specific wavelengths near the wavelength for light emission from the original QW structure. Vacancy diffusion across a heterojunction elicits movement of both group III and group V atomic constituents of the crystal in a manner similar to that observed for concentration-gradient driven diffusion. The result is smearing of abrupt heterojunctions into graded junctions. This grading of the heterojunction, when applied to narrow QW structures, causes square-profile QWs to become parabolic over a limited distance. This shape change of the potential well formed by the heterostructure band edges causes the light-emission energy of direct gap semiconductors, such as AlGaAs, to increase, or "blue-shift". Figure 4.1 shows QW photoluminescence spectra at room temperature for a QW with varying degrees of vacancy-diffusion-induced disordering. Please see the references for a complete discussion of vacancy diffusion and disordering of heterojunctions.

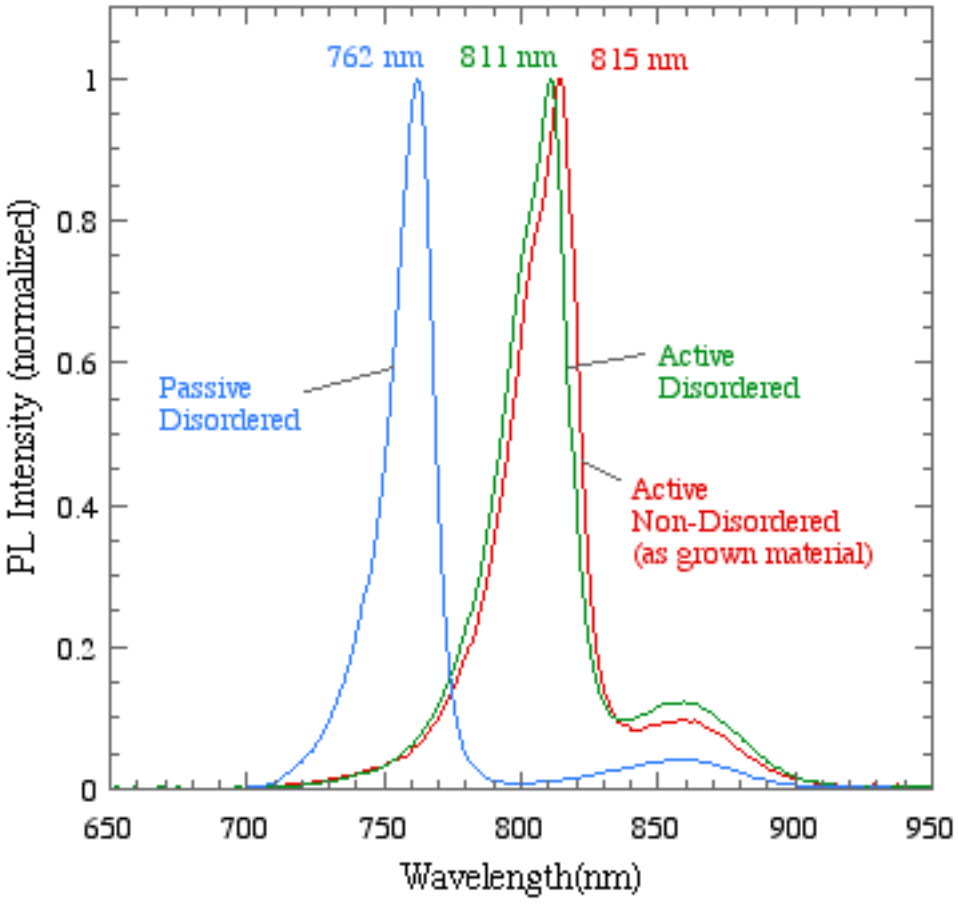

Figure 4.1: Room temperature photoluminescence of disordered and non-disordered quantum wells.

We have applied vacancy diffusion as a means to achieve active-passive integration of semiconductor lasers and non-absorbing interconnecting waveguides. Using nondisordered QW regions as lasers and disordered regions as passive waveguides, the blue-shift of the absorption edge caused by disordering renders the passive waveguides nearly transparent to light emitted by the neighboring lasers.

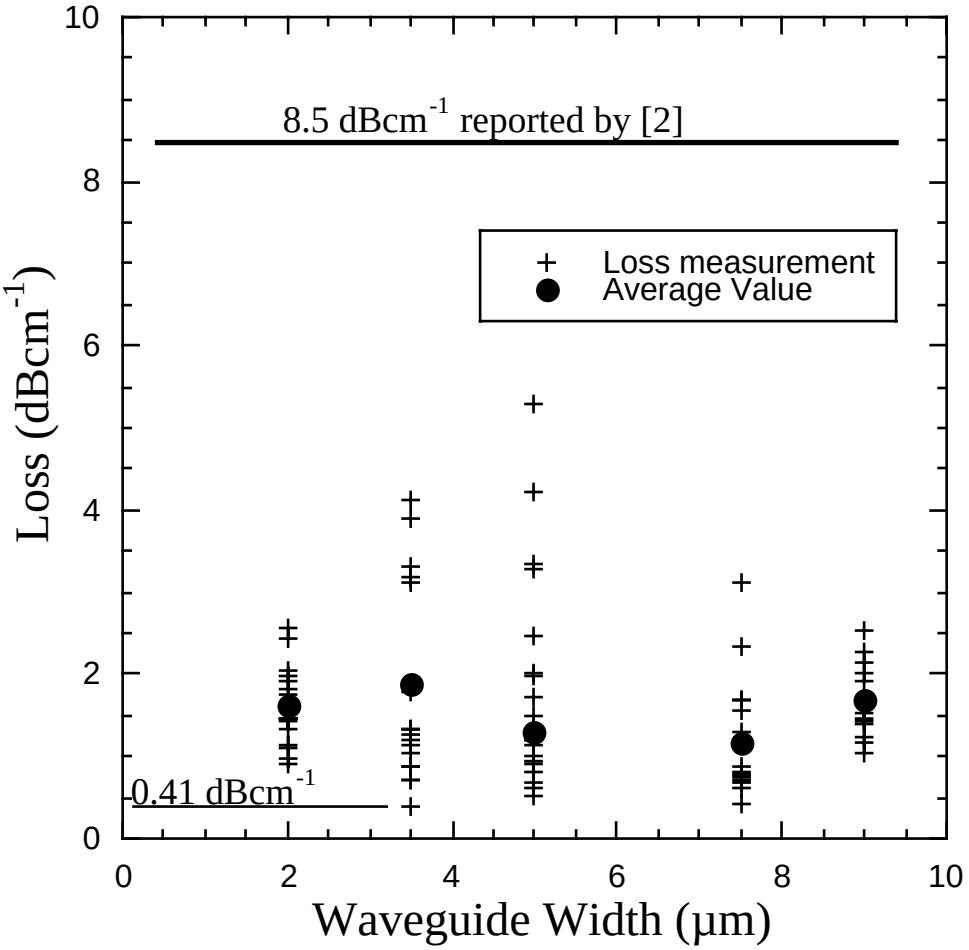

Figure 4.2: Waveguide loss data obtained from 50 nm room temperature photoluminescence blue shifted 60 Å broadened waveguide quantum well material. The waveguide etch depth was 0.9 μm. Waveguide widths ranged from 2 to 9 μm and lengths ranged from 7.8 to 14.1 mm. Data was obtained by the free-space coupled Fabry-Perot temperature tuned method at the non-disordered material's room temperature photoluminescence wavelength of 810 nm.

In this manner, we have achieved record low waveguide loss associated with large photoluminescence blue shifts obtained through impurity free vacancy diffusion (IFVD) of a unique broadened waveguide GRINSCH-SQW [1]. Waveguide loss as low as 0.41 $dBcm^{-1}$ and room temperature photoluminescence blue shifts as large as 76 nm have been measured with this broadened waveguide structure. Reduced free-carrier losses resulting from the broadened waveguide has yielded guided-wave loss measurements averaging less than 2

$dBcm^{-1}$ in material whose room temperature photoluminescence spectrum has been blue shifted 50 nm from the non-disordered material PL peak wavelength of 810 nm, see figure 4.2. In comparison, the lowest loss obtained with IFVD reported in literature was found to be 8.5 $dBcm^{-1}$ [2]. IFVD provides a means of successfully integrating active-passive PIC's in the GaAs/AlGaAs material system [3]. However, the loss values of structures reported in literature are not acceptable for efficient integration. Out effort has been focused on reducing loss of interconnecting waveguides applied to high-density integrated photonics while maintaining acceptable active device performance.

We believe the low-loss measured with this structure is a result of the majority of the optical field being confined within the thick undoped GRINSCH-SQW region. The broadened waveguide structure consists of a single 6 nm quantum well surrounded by 600 nm thick undoped 30%-60% Al grades, see figure 4.3. The optical confinement factor within the broadened waveguide GRINSCH-SQW region is 0.99. For comparison, the confinement factor of a typical GRINSCH structure, defined as a 6 nm quantum well surrounded by 200 nm thick undoped 30%-60% Al grades is 0.84. Using a simple electromagnetic theory, free-carrier loss of the broadened waveguide structure was calculated as 0.0041 $dBcm^{-1}$, compared to 0.44 $dBcm^{-1}$ of the typical GRINSCH. Actual losses are higher due to scattering, phonons, and ionized impurity effects.

t= 50 nm	x= 0.05	p= 2.0E+19	Carbon (CCl_4)
t= 1 nm	x= 0.05	p= 2.0E+19	Carbon (CCl_4)
t= 50 nm	x= 0.05 ramped to 0.6	p= 2.0E+19	Carbon (CCl_4)
t= 500 nm	x= 0.6	p= 2.0E+19	Carbon (CCl_4)
t= 200 nm	x= 0.6	p= 5.0E+17	Carbon (CCl_4)
t= 600 nm	x= 0.3 ramped to 0.6	UID	
t= 6 nm	GaAs quantum well	UID	
t= 600 nm	x= 0.6 ramped to 0.3	UID	
t= 200 nm	x= 0.6	n= 5.0E+17	Silicon (Si_2H_6)
t= 700 nm	x= 0.6	n= 2.0E+18	Silicon (Si_2H_6)
Substrate			

Figure 4.3: Broadened waveguide MOCVD grown GRINSCH quantum well structure. The 60 Å quantum well has 600 nm thick undoped grades. In the figure above, t represents the layer thickness and x represents the Al concentration in $Al_{(x)}Ga_{(1-x)}As$.

For this experiment, one sample was disordered and processed for Fabry-Perot temperature tuned loss measurements and numerous samples were processed as disordering

experiments. The disordered samples were covered with 300 nm of PECVD SiO_2 and non-disordered samples were covered with 300 nm of PECVD SiN_x. Quantum well intermixing occurred during anneals at 900°C for 2-4 minutes. The films were removed in a CF_4/O_2 plasma and room temperature photoluminescence data was obtained. Seventeen disordering experiments resulted in an average room temperature photoluminescence blue shift of 58 nm with a maximum shift of 76 nm. The room temperature photoluminescence blue shifts of the non-disordered regions were typically less than 8 nm.

References:

[1] D. Z. Garbuzov, J. H. Abeles, N. A. Morris, P. D. Gardner, A. R. Triano, M. G. Harvey, D. B. Gilbert, and J. C. Connolly, "High power separate confinement heterostructure AlGaAs/GaAs laser diodes with broadened waveguide," in Proc. SPIE vol. 2682, 20-26.

[2] B. S. Ooi, K. McIlvaney, M. W. Street, A. S. Helmy, S. G. Ayling, A. C. Bryce, J. H. Marsh, and J. S. Roberts, "Selective quantum-well intermixing in GaAs-AlGaAs structures using impurity-free vacancy diffusion," IEEE J. Quantum Electron. **33**, 1784-1793 (1997).

[3] D. Hofstetter, B. Maisenholder, and H. P. Zappe, "Quantum-well intermixing for fabrication of lasers and photonic integrated circuits," IEEE J. Select. Topics in Quantum Electron. **4**, 794-802 (1998).

Distribution:

5 MS 0603 Allen Vawter (1742)
1 MS 0603 Shawn Lin (1743)
3 MS 0603 Charles Sullivan (1742)
1 MS 1077 Tom Zipperian (1740)
1 MS 0601 Weng Chow (1113)
1 MS 0603 Andy Allerman (1742)
1 MS 0603 Walt Zubrzycki (1742)
1 MS 0603 Joel Wendt (1743)
1 MS 0603 Mial Warren (1743)

1 MS 9018 Central Technical Files (8945-1)
2 MS 0899 Technical Library (9616)
1 MS 0612 Review & Approval Desk (9612)
For DOE/OSTI
1 MS 0188 LDRD Office (4001)